UC Berkeley
Building Efficiency and Sustainability in the Tropics (SinBerBEST)

Title

Nonsolvent-induced phase separation synthesis of superhydrophobic coatings composed of polyvinylidene difluoride microspheres with tunable size and roughness

Permalink

Authors

Brockway, Lance
Berryman, Liam
Taylor, Hayden

Publication Date

DOI

Peer reviewed

Nonsolvent-induced phase separation synthesis of superhydrophobic coatings composed of polyvinylidene difluoride microspheres with tunable size and roughness

Lance Brockway[1,2,+,‡], Liam Berryman[1,+,‡], and Hayden Taylor[1,2,*]

[1] Department of Mechanical Engineering,
6159 Etcheverry Hall, University of California, Berkeley, CA 94720

[2] Berkeley Education Alliance for Research in Singapore (BEARS)
CREATE Tower, 1 Create Way, #11-00 Singapore 138602

[*] Corresponding author – telephone: +1 510 642-4901; e-mail: hkt@berkeley.edu

[+] Now with Nelumbo, Inc.

[‡] These authors contributed equally to this work.

Keywords: superhydrophobic; microsphere; NIPS; lotus; PVDF; spinodal decomposition

Abstract

Polyvinylidene difluoride (PVDF) microspheres are synthesized using the non-solvent induced phase separation (NIPS) method. The diameters of the microspheres are varied from 0.3 μm to 2.8 μm by controlling the amount of water added to a solution of PVDF in dimethylformamide. Sphere aggregates are created from spun-on films whose thickness is tuned in the range 6.5–16.5 μm by varying the spin-casting rotational velocity. Spin-casting with optimized parameters results in high-surface-area films that are among the most superhydrophobic non-templated polymer coatings to date, with water contact angles up to 171°, hysteresis less than 12°, and slide angle as low as 3°. We model the dependence of sessile water contact angle on the morphological properties of the films, including not only the sphere diameter, but also nanoscale roughness of the microsphere surfaces and the geometries of macroscopic fingers formed by the aggregated spheres.

1. Introduction

Within the last decade, research into microsphere technologies has progressed to enable a range of applications in fields such as pharmaceuticals [1],[2], biological sensors [3],[4], photonics [5], and, recently, superhydrophobic materials [6]. Further, microspheres with central voids have desirable compressive, acoustic, and tensile properties when organized into syntactic foams [7]–[9]. Research has now begun to focus on enhanced control of these microspheres with the goal of efficient, reliable fabrication of micro-objects possessing desirable bulk or unit performance [10]. Microspheres of several polymers have been realized: Zhang *et al.* recently prepared fluorinated polystyrene (PS) microspheres through distillation precipitation polymerization [11], while poly-epsilon-caprol actone (PCL) microspheres have been thoroughly studied as a degradative delivery vehicle with production methods including emulsion solvent extraction, hot melt, solution-enhanced dispersion, and spray drying [12].

One particularly intriguing methodology for microsphere growth is non-solvent-induced phase separation (NIPS). NIPS describes the process in which a ternary solution of solvent, non-solvent, and polymer components separate into a bi-phase system of polymer-rich and polymer-poor regions [13]. The introduced non-solvent—which is nevertheless miscible with the existing solvent—is the driving force behind the separation, creating a solvent/non-solvent phase which is generally allowed to evaporate from the system [14]. By controlling external parameters, percolation activity of this polymer-poor phase can be altered to introduce unique surface morphologies [15]. Recently, NIPS has been used as a growth procedure for polymer microspheres. Piacentini *et al.* combined membrane emulsification with NIPS to produce polyethersulfone (PES) microspheres [16], while Gao *et al.* leveraged a coupled method of NIPS and electrospray technology to fabricate hierarchically porous polymethyl methacrylate (PMMA) microspheres capable of superhydrophobic performance [17].

Synthetic superhydrophobic surfaces are desirable due to their droplet shedding [18]–[20], anti-sticking [21],[22], and self-cleaning [23]–[25] tendencies, as well as other valuable characteristics [26]. As shown by widespread studies of the lotus leaf [27], [28], a hierarchical, multi-scale surface structure incorporating both micro- and nano-scale features can yield exceptionally desirable hydro-static and -dynamic properties, including water contact angle (θ^*), hysteresis, and slide angle (SA) [29]. One feasible material for mimicking such structures is polyvinylidene difluoride (PVDF), an abundant, inexpensive, and easily malleable thermoplastic fluoropolymer [30]. A flat PVDF surface has been variously reported [31], [32] as having an inherent water contact angle of between 82° and 95°, and this contact angle can be considerably raised by surface roughening and the induction of a composite (*i.e.* Cassie–Baxter [33]) interface in which a small fraction of the solid surface's projected area is in contact with the liquid.

The motivation to produce extremely rough surfaces from PVDF has spurred multiple efforts within the last several years: Zheng *et al.* [34] showed that alkali conditions during chemical bath deposition of PVDF improve θ^* to 155° and SA to 4°, while Wang *et al.* [35] proposed a PTFE/PVDF composite fabricated through mechanical hot press and abrasion with a θ^* greater than 160° and SA less than 5°. Many other methods have returned similar θ^* and SA characteristics [35]–[38]. In addition, there have been several attempts to achieve superhydrophobicity with PVDF–carbon nanotube/graphene composites [39]–[41]. Finally, one of the more promising cost-effective production procedures has been put forth by Peng *et al.*, who showed θ^* of 150° through simple immersion baths [42].

Previous work using the NIPS technique in conjunction with PVDF, however, has focused primarily on porous membrane formation, as opposed to the creation of aggregates of microspheres. Sphere aggregates are expected to be preferable to porous membranes for water repellence, because to achieve low contact-angle hysteresis and slide angle one actually desires a composite (liquid–solid and liquid–air), Cassie–Baxter-like interface with as small a liquid–solid fraction as possible, and spheres that have aggregated to form a surface with many asperities are more likely to offer a low solid-area fraction than an essentially flat membrane perforated by pores. An intermediate morphology composed of spherule-reminiscent

PVDF structures has been observed [43],[44], although no optimization was performed on the material's properties and the highest resultant contact angle was 110°, little different from that of a flat surface [45]. There thus remains a need for a comprehensive investigation of the parameters governing the formation of PVDF microspheres. We provide here the first detailed study of the formation of PVDF microsphere aggregates via NIPS. We demonstrate the ability to control the sphere size and surface roughness to determine overall wettability by modulating the diffusion rate of the solvent. These structures are shown to possess superhydrophobic performance that is superior to any previously reported polymeric material, and have the potential to be cast or sprayed on to any surface.

2. Methods[1]

2.1. Microsphere Synthesis

Aluminum scanning electron microscopy (SEM) sample-mounting pegs were cleaned by sonication in acetone for 15 minutes. A 20 wt% polymer solution was created by dissolving PVDF pellets into dimethylformamide (DMF) in an 80±2 °C water bath for three hours. Quantities of water ranging from 0.06 to 5.51 % of total mass were loaded into the solution. The solution was then vortex-mixed for five minutes. An aluminum SEM peg with diameter 12.7 mm was drop-cast with 50.0 µL of the polymer solution and then spun at between 1100 rpm and 2600 rpm for 30 s. Immediately after spinning, the pegs were submerged in deionized water for 30 minutes at 90±2 °C. After removing the samples from the water, they were air-dried and then pumped under dynamic vacuum at room temperature overnight to ensure that the pores of the resulting polymeric film were free of solvent and water. Aluminum SEM pegs were used purely for convenience and the substrate material is not expected to limit applicability of the coating. Provided that a substrate is flat enough to facilitate spinning and capable of being wetted by the PVDF/DMF solution, the coating is expected to be applicable to the substrate.

2.2. Scanning electron microscopy

After formation and drying, PVDF films were imaged by scanning electron microscopy (FEI Quanta 3D FEG) at 10 kV with a secondary electron detector.

2.3. Sessile Drop Contact Angle, Slide Angle, and Hysteresis Measurements

Sessile drop contact angle measurements were performed using 5 µL droplets dispensed from a Hamilton Model 1710 LT syringe with threaded plunger. Droplets were imaged from the side with a 4X objective (Olympus Plan Achromat), a 30 mm focal-length achromatic doublet (Thorlabs, Newton, NJ), and a CMOS image sensor (Thorlabs DCC1645C) [46]. Contact angle hysteresis was obtained by mounting each sample in turn on to a tilt stage and moving it at a rate of $0.25 \ °s^{-1}$ while imaging a static droplet at ≥15 frames per second. The advancing and receding contact angles were determined from the last video frame captured before droplet motion began. Hysteresis is the difference between advancing and receding angles. Slide angle was determined to be the inclination of the tilt stage at which droplet motion began. Sessile contact angle measurements were extracted from images using the Low-Bond Axisymmetric Drop Shape Analysis (LB-ADSA) analysis package [47], while hysteresis values were obtained using the Dropsnake package [48], both in ImageJ [49]. Values reported for contact angle, slide angle, and hysteresis are the average of five measurements taken at separate locations on a sample. The test liquids used were, in descending order of surface tension, γ, water (γ = 72.8 mN/m [50]), glycerol (γ = 64 mN/m [50]), thiodiglycol (TDG, γ = 54 mN/m [50]), polyethylene glycol diacrylate 700 Da (PEGDA, γ = 42.3 mN/m [51]), dipropylene glyol (DPG, γ = 33.9 mN/m [50]), and methanol (γ = 22.7 mN/m [50]).

---

[1] Materials were obtained from Sigma-Aldrich unless otherwise stated.

2.4. Film thickness measurement

The PVDF films were gently scratched with a razor blade, taking care not to cut into the aluminum substrate, and film thicknesses were then measured using a Dektak 3030 stylus profilometer.

3. Results and discussion

3.1. Dependence of sphere size/roughness and θ^* on water loading

Figure 1 shows scanning electron micrographs of PVDF microsphere clusters that were produced on aluminum substrates. As the water content of the spun-on PVDF solution increases, the sphere size after decomposition decreases. Microspheres with diameters ranging from 3 µm down to 250 nm were fabricated using the NIPS technique and a 20 wt% PVDF solution. This dependence of sphere size on the amount of water added is consistent with previous reports by Matsuyama [52],[53]. By adding more water, the polymer degree of saturation increases and a larger number of smaller particles precipitate upon submersion in the water bath.
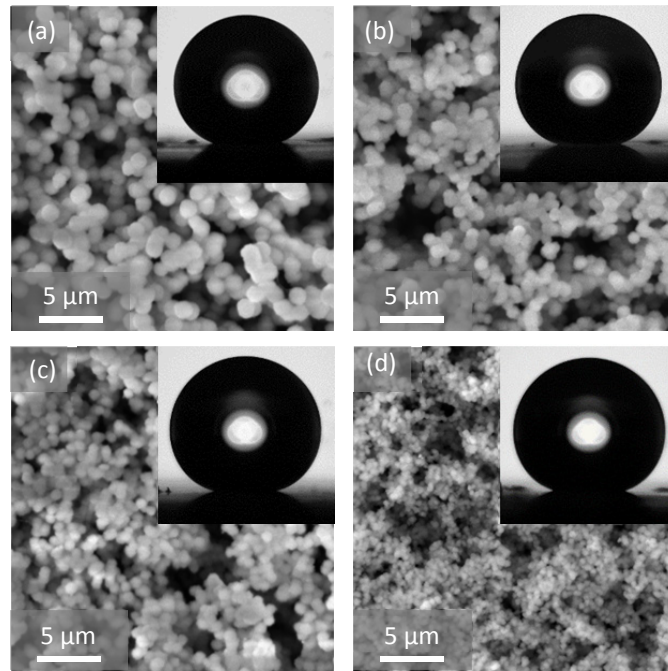
Figure 1. SEM images of PVDF microsphere formations at (a) 0.3%, (b) 0.6%, (c) 1.7%, and (d) 2.8% pre-loaded water. Average sphere diameters range from 1 µm (a) down to 300 nm (d). Inset images show 5.5 µL sessile droplets (diameter ≈ 2 mm) on the respective surfaces. Contact angle measurements were (a) 162°, (b) 166°, (c) 171°, and (d) 169°. Films were spun at 1400 rpm and immersed in water at 90 °C.

Figure 2 shows the relationship between the loaded water fraction and cos θ^*. Meanwhile, Figure 3 shows how the average sphere size depends on water loading fraction. Sphere sizes were extracted from SEM images of the specimens. Taking Figures 2 and 3 together (see also Table 1), we note that for sphere diameters above about 500 nm (occurring for water loadings <2 wt%), θ^* increases (*i.e.* cos θ^* decreases) as the average sphere size reduces. At a water loading of 1.72 wt%, θ^* reaches a peak value of 170.5±1.0°, which is far superior to that of a flat PVDF surface. For the higher water loadings, however, which give rise to sphere sizes below 500 nm, the trend in θ^* reverses, and θ^* begins to decrease with decreasing sphere size. This effect implies that the water mass loading fraction influences properties other

4

than sphere diameter, such as individual spheres' surface roughness or their geometrical arrangements, affecting the wetting properties of the surface in different ways.

Indeed, further inspection of Figure 1 shows that the sizes of individual spheres are not the sole characteristic of these surfaces. The spheres in every case form irregularly shaped clusters interspersed with voids, and the length-scales of these clusters and voids appear to be around 5 µm, regardless of the sphere size. The phase separation process therefore appears to give rise naturally to a multi-scale surface topography. The 'finger-like' arrangements of spheres that form are attributed by Guillen, for example, to the high miscibility of DMF and water [54].

Moreover, when we observe the surfaces of individual spheres, we see that, for example, spheres with diameters around 1.5 µm produced at 0.3 wt% water loading (Figure 4b) are considerably rougher than those with diameters around 0.3 µm produced at 2.8 wt% water loading (Figure 4c). We hypothesize that the higher surface roughness of larger microspheres is a result of shrinkage-induced buckling occurring during phase separation. PVDF dissolved in DMF has a large swelling coefficient [55] of 1.43, indicating that the spheres will be significantly larger in the swollen state than after the DMF diffuses out.

The observations therefore indicate that there are at least three length scales in many of the structures we have produced: within-sphere roughness of <100 nm, sphere sizes of 300 nm to 3 µm, and sphere aggregates and inter-sphere spaces/pores around 5 µm in size.
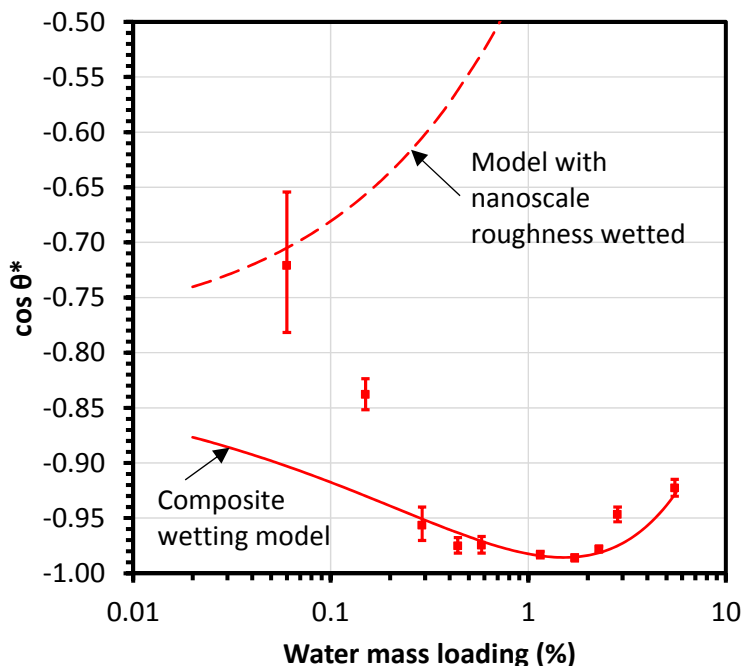
Figure 2. Cosine of sessile apparent water contact angle, cos $\theta*$, versus loaded water as a percentage of total mass. A spin angular velocity of 1400 rpm and a submersion bath temperature of 90 °C were used. The peak $\theta*$ measured was 170.5±0.9° for a sphere diameter of 652±65 nm achieved at 1.72% water loading. Error bars correspond to ±1 standard deviation of five separate measurements on each specimen. In some cases symbols are larger than error bar lengths. Uncertainty in water mass loading is less than 2%. Solid line: full composite wetting model as described in text. Dashed line: model with spheres completely wet at the nanoscale.
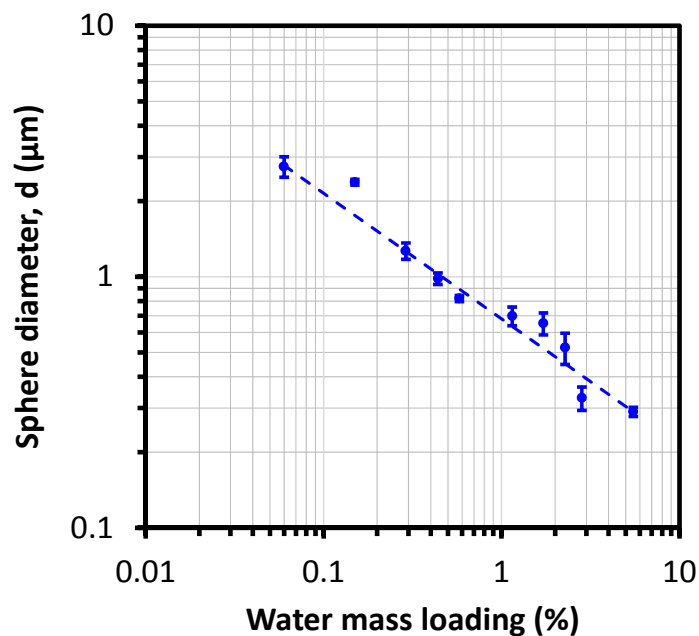
Figure 3. Sphere diameters versus loaded water as a percentage of total mass for the results shown in Figure 2 above. Error bars show ±1 standard deviation of five separate measurements from a scanning electron micrograph of each specimen. In some cases symbols are larger than error bar lengths. Dashed line: inverse-square-root model for sphere diameter as a function of water loading.

Table 1. Sessile apparent water contact angles and PVDF sphere sizes as a function of pre-decomposition water loading in the film.

Water wt%	Sessile apparent water contact angle (°)		PVDF sphere size (µm)	
	Average	Std. dev.	Average	Std. dev.
0.06	136.1	5.28	2.75	0.26
0.15	146.9	1.47	2.38	0.06
0.29	163.0	2.98	1.27	0.09
0.44	167.2	1.81	0.98	0.05
0.58	167.1	1.94	0.82	0.02
1.15	169.5	0.99	0.70	0.06
1.72	170.5	0.95	0.65	0.07
2.28	168.0	0.76	0.52	0.07
2.83	161.2	1.20	0.33	0.04
5.51	157.3	1.14	0.29	0.01
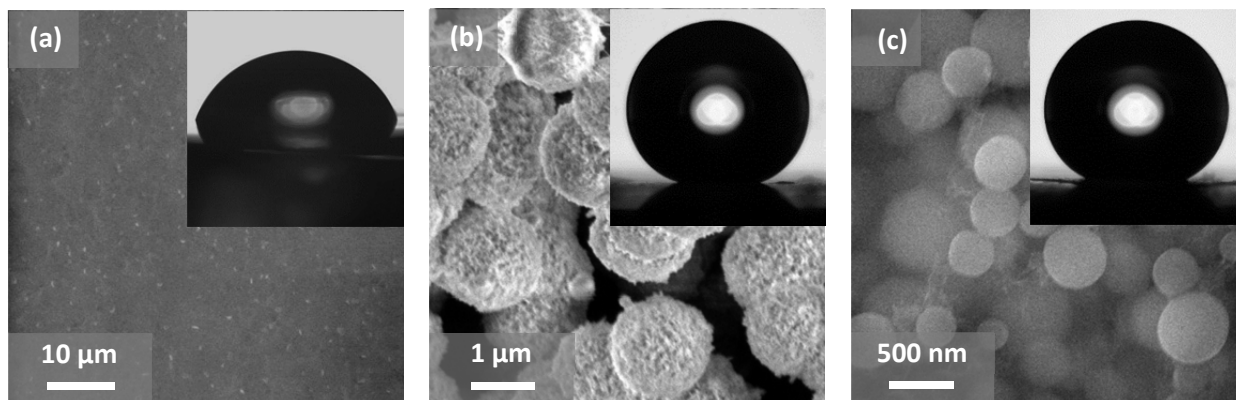
Figure 4. A smooth PVDF film cast from the melt (a) shows a sessile water contact angle of 79±4° (based on five measurements). In the spinodal decomposition process, sphere size and roughness depend on the initial water loading: larger spheres (b), produced with 0.3 wt% water loading, 1400 rpm spin speed, and a 90 °C water bath, exhibit rough surfaces, while smaller spheres (c), produced at 2.8% water loading under otherwise identical conditions, remain relatively smooth.

3.2. Dependence of θ^* on film thickness

We have also explored how the sessile water contact angle depends on spun-on film thickness. Figure 5a shows that thicker films correspond to higher θ^*, with cos θ^* falling approximately linearly with increasing thickness (see also Table 2). This trend indicates that a water droplet in contact with the film is unlikely to be confined to its top boundary, but rather infiltrates the pores to some extent. The data also suggest that films produced with a 1.72% water loading maintain a higher contact angle than those with 0.58% loading, across almost the full range of film thicknesses explored, with the exception of the very thickest films. This observation implies that the sizes and textures of individual microspheres are reasonably insensitive to the overall thickness of the film.

The film thickness itself is controlled by varying the spin speed during deposition of the PVDF/DMF/water mixture, and Figure 5b indicates that the thickness–spin speed relationship is insensitive to the water loading fraction for the two values used. Given the small percentage of water used, it is unsurprising that the solution's viscosity, and hence the spun-on film thickness, is insensitive to the water content.
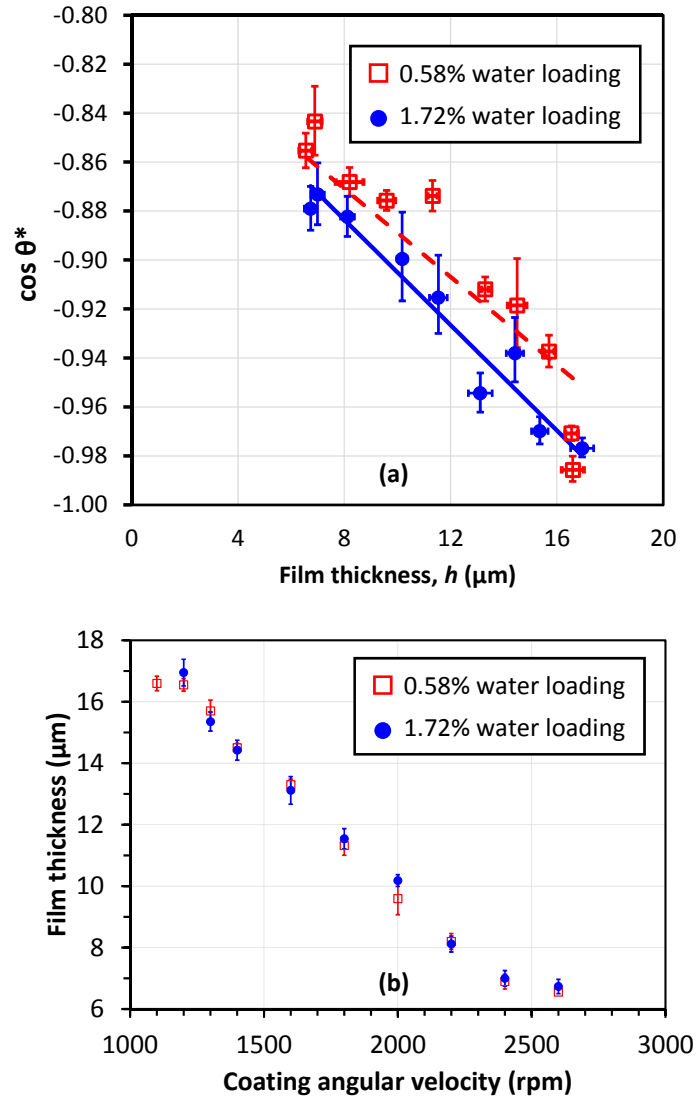
Figure 5. (a) Cosine of apparent sessile water contact angle θ^* *vs* film thickness for samples immersed in 90 °C water for 30 minutes. An increase in contact angle is observed with increasing film thickness. Symbols show experimental results; lines show the model fit as described in the text. **(b)** Measured film thickness *vs* spinning speed after a 30 s spin, indicating tight control over film thickness ranging from 6 µm to 16 µm, independent of water loading. Error bars on the film thickness indicate ± 1 standard deviation of three separate profilometer measurements on a single sample. Error bars on $\cos \theta^*$ indicate ± 1 standard deviation of five separate droplet measurements on each sample.

Table 2. Measured film thicknesses and sessile apparent θ^* versus spin speed for films with two different water loading concentrations. (For 1100 rpm and 1.72wt% water loading, the film thickness was not measured.)

Spin speed (rpm)	0.58 wt% water loading				1.72 wt% water loading			
	Film thickness (µm)		Sessile apparent water contact angle, θ^* (°)		Film thickness (µm)		Sessile apparent water contact angle, θ^* (°)	
	Average	Std. dev.	Average	Std. dev.	Average	Std. dev.	Average	Std. dev.
1100	16.6	0.4	170.3	1.8	-	-	171.5	1.5
1200	16.6	0.2	166.1	0.7	17.0	0.4	167.7	1.5
1300	15.7	0.2	159.6	1.1	15.4	0.3	165.9	3.1
1400	14.5	0.3	156.7	2.6	14.4	0.3	159.7	1.3
1600	13.3	0.1	155.8	0.7	13.1	0.4	162.6	3.1
1800	11.3	0.2	150.9	0.7	11.5	0.3	156.3	2.6
2000	9.6	0.3	151.1	0.5	10.2	0.2	154.1	1.1
2200	8.2	0.5	150.2	0.7	8.1	0.3	151.9	1.5
2400	6.9	0.3	147.5	1.5	7.0	0.3	150.8	1.1
2600	6.6	0.2	148.8	0.8	6.7	0.2	151.5	0.6

3.3. A model for liquid–surface interaction

To explain the relationship between the PVDF morphologies and their θ^* values, we adapt our previously reported approach to modeling irregular porous or rough surfaces [46]. Because these PVDF structures contain at least three different length-scales — from the nanoscale roughness of individual microspheres to the pores defined by aggregated spheres — we add a further level of geometry to our previous model.

We use a modified Cassie–Baxter model [33] in which the cosine of the apparent contact angle, $\cos \theta^*$, is the area-weighted average of the cosines of contact angles associated with each portion i of a composite, partially wetted interface. A_i is the fraction of the total projected surface area occupied by material making a contact angle of θ_i with the liquid:

$$\cos \theta^* = \sum_i A_i \cos \theta_i \quad \text{where} \quad \sum_i A_i = 1. \tag{1}$$

The area fractions A_i are components of the *projected* surface area and by definition sum to 1. A component may, however, as discussed below, contain roughness that makes its true surface area higher than its projected area and determines the associated value of $\cos \theta_i$. At the largest length-scale in our PVDF surfaces, there are three different components of the composite interface, as illustrated in Figure 6a and described in Equation 2:

$$\cos \theta^* = \phi_{T,\mu} \cos \theta_1 + (1 - \phi_{T,\mu})[\phi_f \, r_\mu \cos \theta_1 - (1 - \phi_f)]. \tag{2}$$

The first term in Equation 2 ($\phi_{T,\mu} \cos \theta_1$) is associated with the fraction $\phi_{T,\mu}$ of the surface's total projected area that is occupied by the tips of the sphere aggregates. This region is considered always to be in contact with the liquid and, like the rest of the surface, is composed of aggregated microspheres. The

contact angle associated with this region, θ_1, is the effective contact angle of the liquid on a composite liquid–PVDF/liquid–air interface that is created by the nanoscale roughness of the sphere surfaces. The modeling of θ_1 is discussed further below.

The remaining fraction $1 - \phi_{T,\mu}$ of the overall surface contains pores defined by the aggregated microspheres. As noted above, these pores are several micrometers wide and are highly irregular in shape and size. This irregularity includes variation of the effective sidewall angle, Ψ, meaning that a liquid with a particular surface tension will be drawn into some pores but not others. Hence, a fraction ϕ_f of the pores are considered filled with liquid and $1 - \phi_f$ of them not filled.

In the pores that are filled, the liquid is in contact with the rough pore walls defined by the sphere aggregates and, at the microscale, these pores have a surface roughness r_μ, which is the ratio of the microscopic surface area of a pore to its projected area. The sphere surfaces, meanwhile, frequently have a nanoscale roughness, and their local contact angle θ_1 again represents the effect of a nanocomposite liquid–PVDF/liquid–air interface. Hence, following the Wenzel relation [56] at the microscale within the filled pores, the cosine of the effective contact angle contributed by the pore walls is modeled as $r_\mu \cos \theta_1$.

Finally, above those pores that are not filled, there is a purely liquid–air interface which by definition has an effective 'contact angle' cosine of -1; the last term inside the square brackets in Equation 2 is contributed by this interface.
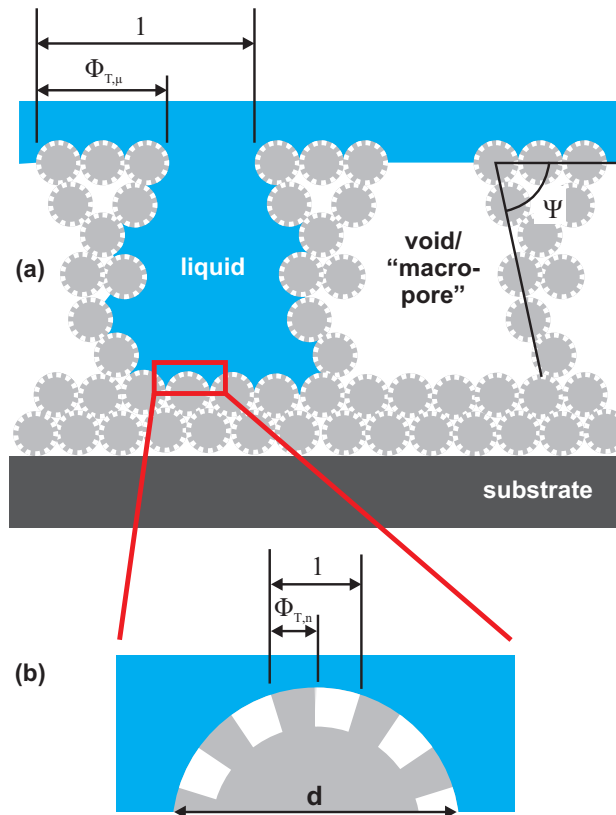
Figure 6. Schematic showing model parameters for the PVDF microsphere films. In our conception of the partial wetting of these surfaces, sphere aggregates create macroscopic pores (a), some of which are filled with liquid and others not, while individual spheres (b) have a degree of nanoscale roughness and experience composite wetting.

10

To complete the model, we need to explain how r_μ, θ_1 and ϕ_f are modeled. To model r_μ, we observe that the volume of PVDF per unit projected area of film is $f_v h$ where f_v is the volume fraction of PVDF in the solution (11.7 vol% for the 20 wt% solution used) and h is the spun-on film thickness. We assume that sphere diameters are monodisperse for a particular set of processing conditions. Spheres with diameter d each have volume $\pi d^3/6$, so the number N of spheres per unit projected film area is:

$$N = \frac{6f_v h}{\pi d^3} \tag{3}$$

Each sphere has surface area πd^2, and if the spheres were to be uniformly dispersed so that their full surface area were able to make contact with liquid, the roughness would be:

$$r_\mu = \frac{6f_v h}{d} \tag{4}$$

In reality, of course, as Figures 1 and 4 show, aggregated spheres do touch each other and fuse to produce a film with mechanical integrity. We therefore introduce a 'merging' parameter, $0 < m < 1$, which reduces the microscale roughness to:

$$r_\mu = \frac{6f_v m h}{d} \tag{5}$$

This model predicts that microscale roughness increases proportionally with film thickness h and is inversely proportional to sphere diameter d. In turn, Equation 2 shows that, provided $\cos\theta_1 < 0$, increasing r_μ correlates with a more negative $\cos\theta^*$ and therefore higher θ^*. Equation 5 therefore provides a basis for understanding most of the experimental observations in Figure 2 and Figure 5a. It does not, however, explain the reduction in θ^* that is seen in Figure 2 for water loading fractions above 1.72 wt%. A possible explanation for this falling-off of θ^* can be seen in Figure 4, where the smallest spheres appear to have less *nanoscale* roughness than larger ones. The degree of *nanoscale* roughness of each microsphere's surface is a distinct factor from the *microscale* roughness of the pores, which results from microspheres' diameters and geometrical arrangements and is modeled using Equations 3–5 above. We hypothesize that the microspheres that do exhibit a nanoscale surface roughness experience a Cassie–Baxter composite wetting mode, while those without significant surface roughness experience closer to full surface wetting and consequently a less negative value of $\cos\theta_1$.

Our model for θ_1 therefore draws upon three observations: (*a*) since thicker films, in which a greater number of microspheres are expected to interact with the liquid, exhibit higher contact angles, it follows that $\cos\theta_1 < 0$; (*b*) since θ_0, the liquid's contact angle on a flat PVDF surface, is below 90° ($\theta_0 = 79\pm4°$ for water, as seen in Figure 4a), there must be a composite wetting mode at the surfaces of the microspheres, involving some liquid–air interfaces, to achieve $\cos\theta_1 < 0$; (*c*) since the smoothest microspheres yield a lower overall contact angle than slightly larger, rougher spheres, the model for $\cos\theta_1$ needs to capture the weakening of the composite mode at the smallest sphere sizes.

To reflect these three observations, the nanoscale roughness is regarded as a series of asperities that cover a fraction $\phi_{T,n}$ of each microsphere's surface area (Figure 6b). The liquid is regarded as making contact only with these asperities and so, following the same principle as in Equation 1, the effective local contact angle is modeled as:

$$\cos\theta_1 = \phi_{T,n}\cos\theta_0 - (1 - \phi_{T,n}) = \phi_{T,n}(1 + \cos\theta_0) - 1. \tag{6}$$

The curvature of the microspheres themselves is neglected here because it is far gentler than that of the nanoscale asperities covering the spheres. It should be noted that since $\theta_0 < 90°$ this envisaged composite

11

wetting state is metastable, and a possibility exists for a Cassie-to-Wenzel transition at the nanoscale, whereby the entire solid surface of at least some of the microspheres could become wetted, in response, for example, to mechanical vibration or the kinetic energy of an impinging droplet.

The hypothesized weakening of the composite mode — and hence the reduction of θ^* — as microspheres become very small is captured with a two-parameter phenomenological function for $\phi_{T,n}$:

$$\phi_{T,n} = \phi_{T,n0} + \phi_{T,n1} \log d \tag{7}$$

where d is in μm. For a negative value of $\phi_{T,n1}$, this function represents an expanding liquid–solid contact area fraction with reducing sphere size. Sphere diameter, meanwhile, is empirically related to the water loading concentration C (in wt%) by:

$$d = d_0 C^{d_1} \tag{8}$$

where d_0 and d_1 are fitting parameters. This relationship captures the dependence of the kinetics of the spinodal decomposition upon the water loading concentration, C.

The last component of the model to be defined is ϕ_f. As in our previous work [46], we go beyond the traditional provisions of the Cassie–Baxter or Wenzel models by allowing for the possibility of only a fraction of pores, $0 < \phi_f < 1$, being filled with liquid. In our previous work we assumed a simple Gaussian distribution of pore sidewall re-entrant angle Ψ, with a pore filling with liquid only where the microscopic contact angle (here, θ_1) was less than the local Ψ. This model was found to work well for hydrothermally grown zinc oxide [57] among other surfaces [46]. In the case of the PVDF surfaces, however, we deduce from Figure 5a that even with water, the least-wetting of the fluids tested, a substantial fraction of the pores are filled because θ^* depends strongly on the thickness of the film. We therefore describe what appears to be a highly skewed distribution of effective Ψ by modifying the cumulative distribution function for ϕ_f (Equation 9) to include a 'base' fraction of pores, ϕ_{f0}, that are always filled, with a Gaussian distribution of pore sidewall angle (mean Ψ_f, standard deviation σ_f) determining how many of the remaining fraction $(1 - \phi_{f0})$ of pores are also filled:

$$\phi_f(\theta_1) = \phi_{f0} + (1 - \phi_{f0}) \int_{-\infty}^{\theta_1} \frac{1}{\sigma_f \sqrt{2\pi}} e^{-\left[\frac{(\theta - \Psi_f)^2}{2\sigma_f^2}\right]} d\theta \tag{9}$$

To fit values for the model parameters, we begin by fitting d_0 and d_1 to directly measured sphere diameter values (Figure 3). We find that an inverse-square-root model ($d_1 = -0.5$) fits the results very closely. The negative value of the exponent d_1 is consistent with the physical effect that as water loading increases, more water molecules are available to serve as nucleation sites for decomposition, and thus, for a given PVDF concentration, the average size of the PVDF spheres is reduced.

We then obtain an initial guess for ϕ_{f0} by noting that the trends in Figure 5a, when extrapolated, intersect the $h = 0$ axis at $\cos \theta^* \approx -0.8$. By temporarily assuming $\phi_{T,\mu} \approx 0$ and $r_\mu \approx 0$ at $h = 0$, Equation 2 simplifies to give $\phi_f \approx 0.2$, and we assume that for water, a minimal number of pores are filled compared to other possible liquids, so that $\phi_{f0} \approx \phi_f$.

Next, the *form* of the phenomenological function for $\phi_{T,n}$ (Equation 7) and initial estimates of $\Phi_{T,n0}$ and $\Phi_{T,n1}$ are deduced by rearranging Equation 2 to give $\cos \theta_1$ in terms of $\cos \theta^*$ and other variables, taking $\phi_f = 0.2$, $m = 0.8$, and $\phi_{T,\mu} = 0$, and plotting $\cos \theta_1$ against d for the data in Figure 2. Then, the final values of ϕ_{f0}, $\phi_{T,\mu}$, m, $\Phi_{T,n0}$, and $\Phi_{T,n1}$ are arrived at by iteratively varying these parameters until the

12

root mean square differences between the model and the data in Figure 2 and Figure 5a are minimized. The results of this fitting procedure are shown in Table 3. The final relationship between $\cos\theta_1$ and d is shown in Figure 7 for the water loading dependence experiments.

The fitting error is particularly sensitive to variations in m, $\Phi_{T,n0}$ and $\Phi_{T,n1}$. The experimental studies of water-loading dependence (Figure 2) and film-thickness dependence (Figure 5a) were conducted on separate occasions, and small run-to-run fluctuations in, for example, the temperature of the immersion water bath (approximately ±2 °C) could have been enough to perturb the effective values of these parameters. Slightly different values of these parameters are therefore fit for the two experimental studies.
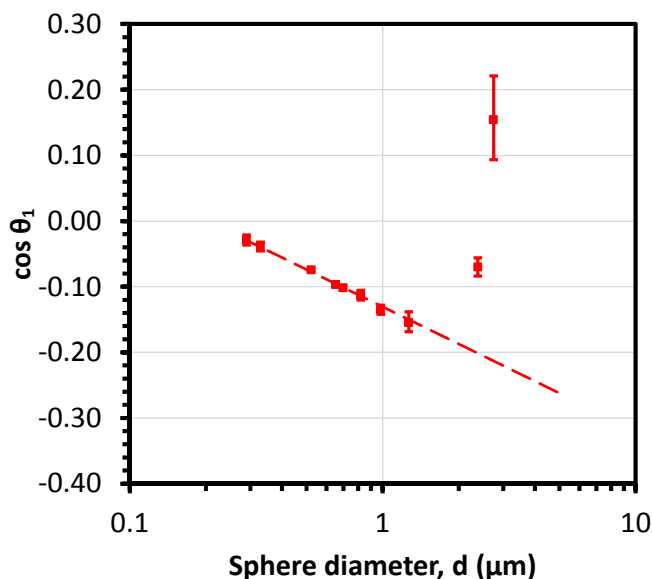
Figure 7. Modeling of $\cos\theta_1$ vs sphere diameter, d, for the results in Figures 2 and 3 and Table 1. For the largest two sphere sizes, $\cos\theta_1$ deviates from the composite model of Equation 7 and approaches the value of $\cos\theta_0 = 0.19$, as extracted from Figure 4a, supporting the idea that those larger microspheres may tend to be in a fully wetted state.

The model represents well the linear reduction of $\cos\theta^*$ with increasing h (Figure 6a). Meanwhile, figures 2 and 8 show that for water loadings of 0.29% and above, the model corresponds closely to the experimental results. For the smallest two water loadings, the model over-predicts θ^*. One possible explanation for the difference is that in these two cases a Cassie-to-Wenzel transition spontaneously and repeatedly occurs, causing the entire surface area of the microspheres to become wetted. As noted above, a partial-wetting mode is metastable if the material's intrinsic surface chemistry is wetting ($\cos\theta_0 > 0$), which is the case with PVDF. These two data points correspond to the largest two microsphere sizes, and the interstices between the spheres are also correspondingly larger, as may be the nanoscale asperities on the spheres. It is plausible in the light, for example, of Tuteja's analysis [58] that these larger structures would be less robust against spontaneous wetting.

In Figure 2, we also plot the model output of Equation 2 for a hypothetical case where the microspheres are completely wetted (*i.e.*, $\Phi_{T,n} = 1$ in Equation 7). For this hypothetical case we assume that the nanoscale roughness of the microspheres' surfaces is very close to 1 so that we can make the approximation $\cos\theta_1 = \cos\theta_0$. The experimental data are well bounded by these alternative model assumptions of partial and full microsphere wetting. (If nanoscale roughness were substantially greater

13

than 1, $\cos\theta_1$ would exceed $\cos\theta_0$ in the full-wetting case, and the experimental data would still be well bounded by the full- and partial microsphere wetting assumptions.)

Table 3. Fit parameters and r.m.s. error for the sessile $\theta*$ model developed in the text.

Variable	Meaning	Water loading dependence study	Spin speed dependence study
$\Phi_{T,\mu}$	Areal fraction of projected film surface in contact at tips of macroscopic pores	0.05	
m	Factor capturing surface area reduction as a result of sphere fusion in film	0.80	0.73
d_0	Coefficient in model for sphere diameter	0.69 µm	
d_1	Exponent in model for sphere diameter	−0.5	
$\Phi_{T,n0}$	First parameter in model for nanoscale roughness	0.730	0.750
$\Phi_{T,n1}$	Second parameter in model for nanoscale roughness	−0.158	−0.109
Φ_{f0}	Lower limit of the fraction of macroscopic pores filled	0.2	
Ψ_f	Effective average re-entrant angle of macroscopic pores	83°	
σ_f	Standard deviation of re-entrant angle of macroscopic pores	1°	
	Root mean square error of model for $\cos\theta*$	0.0107	0.0144

Next, we consider the performance of the model for other probe liquids with lower surface tension and thus a greater propensity to wet the surface. The two model parameters not previously fit are Ψ_f and σ_f. From the plot of $\cos\theta^*$ against $\cos\theta_0$ in Figure 8, we see that there is a sharp transition from little wettability to strong wetting when $0.41 < \cos\theta_0 < 0.53$. This transition implies a tight distribution of effective pore sidewall angles Ψ, which is somewhat surprising given the highly irregular shapes of the pores. We choose $\cos\theta_0 = 0.45$ as the transition point, and, for the sample probed in Figure 8, which has a sphere size of around 0.65 µm and therefore a modeled $\Phi_{T,n}$ of 0.77, a value of $\cos\theta_0 = 0.45$ corresponds to $\cos\theta_1 = 0.12$; *i.e.* $\theta_1 = 83$ °. Given the sharp transition, we set σ_f to the small nominal value of 1 °. The model does represent the transition from non-wetting to wetting as the surface tension of the probe liquid reduces, but the second term in Equation 2, which is proportional to $\cos\theta_0$, contributes to a higher than realistic value of $\cos\theta^*$ for glycerol.
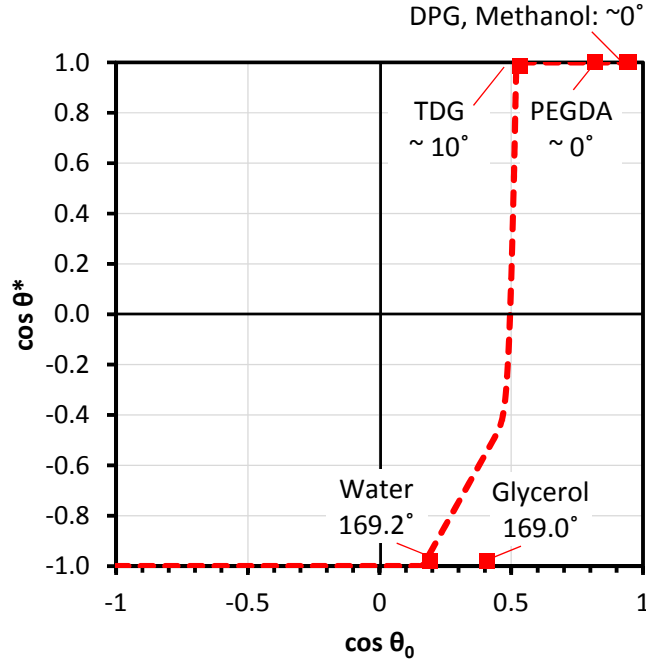
Figure 8. A plot of the cosine of the sessile apparent contact angle, θ^*, against the smooth surface contact angle, θ_0, for six test liquids ranging in surface tension from water to methanol (see Methods for details). The sharp transition from wetting to non-wetting at $\theta_0 \approx 60°$ (*i.e.* $\theta_1 \approx 83$ °) suggests a tightly distributed effective re-entrant angle for the pores of the microsphere-based film. The sample used here was produced at 1200 rpm and 1.7 wt% water loading, with a 90 °C immersion bath. Data points for dipropylene glyol and methanol overlap. Numerical data can be found in [46]. Labels show mean values of θ^*.

3.4. Slide angle and hysteresis: correlations with θ^*

While our model for sessile contact angle provides insight into the PVDF films' structure, θ^* alone cannot fully define the performance of a liquid-repellent surface. The ability of a droplet of liquid to roll or slide across the surface is also important in determining the material's usefulness: smaller hysteresis and slide angles indicate a greater capacity to shed impinging liquid.

Figure 9 shows water contact angle hysteresis and slide angle measurements against sessile θ^* for the five specimens that exhibited an average sessile θ^* above 167°. All of these hysteresis values are considerably smaller than the hysteresis of water on a flat PVDF surface of 38.5°, as measured by Bormashenko using a similar technique [59]. A negative correlation between hysteresis and sessile contact angle is consistent with the model developed by McHale [60] for a Cassie–Baxter composite wetting mode, in which the liquid contacts only the upper asperities of a surface and does not penetrate its pores. In our previous work characterizing silanized hydrothermal zinc oxide [57], we showed that even when some of the pores in a porous surface are fully wetted, provided the fraction of wetted pores is low, McHale's negative correlation between θ^* and hysteresis can still hold, albeit with a greater magnitude of the slope. Taken together, these facts support the picture that the microsphere-based PVDF structures with sessile θ^* values above 167° are penetrated by water in only a small fraction of their area. These structured films certainly offer superior droplet shedding to a flat PVDF surface.

Surfaces with sessile θ^* values lower than 167°, meanwhile, exhibit strong droplet pinning and do not yield measurable hysteresis or slide angle values, supporting the explanation embodied in our model that lower contact angles correspond to a greater degree of wetting of the micro- and nano-structures within the films.

15
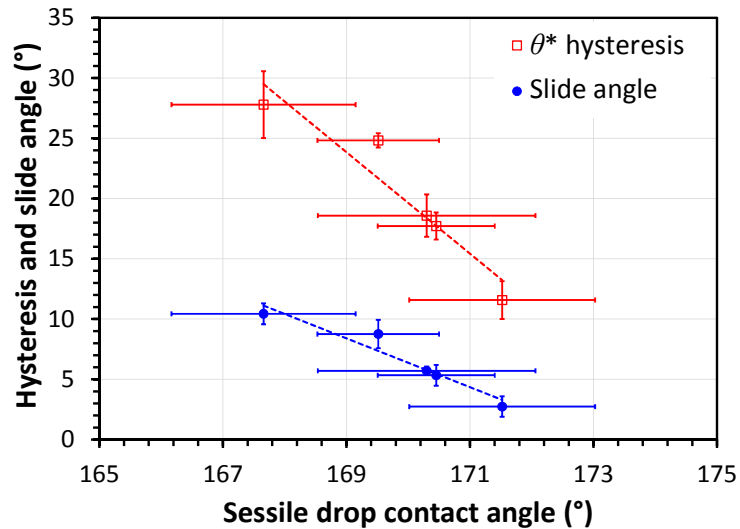
Figure 9. Sessile apparent water contact angle *vs* hysteresis and slide angle, indicating a strong linear decrease in adhesion forces with increasing contact angle. Error bars represent ± one standard error of the mean based on five separate measurements on each specimen. Dotted lines are to guide the eye.

4. Conclusions

- PVDF films composed of microsphere aggregates have been demonstrated. These films contain at least three length-scales of structure, including the microspheres themselves ranging from approximately 0.3 μm to 2.8 μm in diameter, as well as nanoscale roughness on the spheres, and voids that are multiple micrometers in size between clusters of spheres.
- The films are produced using a spinodal decomposition method that involves simply spinning a PVDF/DMF/water solution on to a substrate and immersing in a heated water bath.
- Higher water loading in the spun-on solution yields smaller average PVDF microsphere diameters.
- The highest sessile water contact angle of 170.5±1.0° is obtained for 1.72 wt% water loading in a 20 wt% PVDF solution in DMF, spun at 1400 rpm resulting in a film of 14.5 μm thickness, and followed by a 90 °C water bath immersion. The sphere diameter at this optimal condition is about 0.65 μm.
- The highest sessile water contact angles correspond to the lowest values of contact angle hysteresis and droplet slide angle. Contact angle hysteresis of the optimally performing surface is considerably lower than that reported elsewhere for a flat PVDF surface (11.5 ° *cf.* 38.5°). These results suggest that the optimal surface could find valuable applications in water droplet shedding.
- Sessile contact angles of 168.9±0.9° were also obtained on this optimal surface using glycerol. Other probe liquids with lower surface tensions wetted the surface completely.
- A multi-scale model has been introduced that closely describes the dependence of sessile water contact angle on film thickness and microsphere diameter.

16

References

[1] S. Freiberg and X. X. Zhu, "Polymer microspheres for controlled drug release.," *Int. J. Pharm.*, vol. 282, no. 1–2, pp. 1–18, Sep. 2004.

[2] V. Lassalle and M. L. Ferreira, "PLA nano- and microparticles for drug delivery: an overview of the methods of preparation.," *Macromol. Biosci.*, vol. 7, no. 6, pp. 767–83, Jun. 2007.

[3] X.-J. Huang *et al.*, "Morphology-controlled SWCNT/polymeric microsphere arrays by a wet chemical self-assembly technique and their application for sensors," *Nanotechnology*, vol. 17, no. 12, pp. 2988–2993, Jun. 2006.

[4] N. Bock, M. A. Woodruff, D. W. Hutmacher, and T. R. Dargaville, "Electrospraying, a Reproducible Method for Production of Polymeric Microspheres for Biomedical Applications," *Polymers*, vol. 3, no. 4, pp. 131–149, Jan. 2011.

[5] S. Okamoto, K. Inaba, T. Iida, H. Ishihara, S. Ichikawa, and M. Ashida, "Fabrication of single-crystalline microspheres with high sphericity from anisotropic materials.," *Sci. Rep.*, vol. 4, p. 5186, Jan. 2014.

[6] J. Gao, J. S.-P. Wong, M. Hu, W. Li, and R. K. Y. Li, "Facile preparation of hierarchically porous polymer microspheres for superhydrophobic coating," *Nanoscale*, vol. 6, no. 2, pp. 1056–1063, Dec. 2014.

[7] D. K. Balch, J. G. O'Dwyer, G. R. Davis, C. M. Cady, G. T. Gray, and D. C. Dunand, "Plasticity and damage in aluminum syntactic foams deformed under dynamic and quasi-static conditions," *Mater. Sci. Eng. A*, vol. 391, no. 1–2, pp. 408–417, Jan. 2005.

[8] H. S. Kim and H. H. Oh, "Manufacturing and impact behavior of syntactic foam," *J. Appl. Polym. Sci.*, vol. 76, no. 8, pp. 1324–1328, May 2000.

[9] L. Zhang and J. Ma, "Effect of coupling agent on mechanical properties of hollow carbon microsphere/phenolic resin syntactic foam," *Compos. Sci. Technol.*, vol. 70, no. 8, pp. 1265–1271, Aug. 2010.

[10] Y. Ning, C. Wang, T. Ngai, and Z. Tong, "Fabrication of tunable Janus microspheres with dual anisotropy of porosity and magnetism.," *Langmuir ACS J. Surf. Colloids*, vol. 29, no. 17, pp. 5138–44, Apr. 2013.

[11] D. Zhang, J. Liu, T. Liu, and X. Yang, "Synthesis of superhydrophobic fluorinated polystyrene microspheres via distillation precipitation polymerization," *Colloid Polym. Sci.*, vol. 293, no. 6, pp. 1799–1807, Mar. 2015.

[12] V. R. Sinha, K. Bansal, R. Kaushik, R. Kumria, and A. Trehan, "Poly-epsilon-caprolactone microspheres and nanospheres: an overview.," *Int. J. Pharm.*, vol. 278, no. 1, pp. 1–23, Jun. 2004.

[13] D.-M. Wang and J.-Y. Lai, "Recent advances in preparation and morphology control of polymeric membranes formed by nonsolvent induced phase separation," *Curr. Opin. Chem. Eng.*, vol. 2, no. 2, pp. 229–237, May 2013.

[14] G. R. Guillen, Y. Pan, M. Li, and E. M. V. Hoek, "Preparation and Characterization of Membranes Formed by Nonsolvent Induced Phase Separation: A Review," *Ind. Eng. Chem. Res.*, vol. 50, no. 7, pp. 3798–3817, Apr. 2011.

[15] X. Li, Y. Wang, X. Lu, and C. Xiao, "Morphology changes of polyvinylidene fluoride membrane under different phase separation mechanisms," *J. Membr. Sci.*, vol. 320, no. 1–2, pp. 477–482, Jul. 2008.

[16] E. Piacentini, D. S. Lakshmi, A. Figoli, E. Drioli, and L. Giorno, "Polymeric microspheres preparation by membrane emulsification-phase separation induced process," *J. Membr. Sci.*, vol. 448, pp. 190–197, Dec. 2013.

[17] J. Gao, W. Li, J. S.-P. Wong, M. Hu, and R. K. Y. Li, "Controllable morphology and wettability of polymer microspheres prepared by nonsolvent assisted electrospraying," *Polymer*, vol. 55, no. 12, pp. 2913–2920, Jun. 2014.

[18] J. Boreyko and C.-H. Chen, "Self-Propelled Dropwise Condensate on Superhydrophobic Surfaces," *Phys. Rev. Lett.*, vol. 103, no. 18, p. 184501, Oct. 2009.

[19] N. Miljkovic, R. Enright, and E. N. Wang, "Effect of droplet morphology on growth dynamics and heat transfer during condensation on superhydrophobic nanostructured surfaces.," *ACS Nano*, vol. 6, no. 2, pp. 1776–85, Feb. 2012.

[20] A. Nakajima, "Design of hydrophobic surfaces for liquid droplet control," *NPG Asia Mater.*, vol. 3, no. 5, pp. 49–56, May 2011.

[21] B. Bhushan and Y. C. Jung, "Natural and biomimetic artificial surfaces for superhydrophobicity, self-cleaning, low adhesion, and drag reduction," *Prog. Mater. Sci.*, vol. 56, no. 1, pp. 1–108, Jan. 2011.

[22] B. Bhushan, K. Koch, and Y. C. Jung, "Nanostructures for superhydrophobicity and low adhesion," *Soft Matter*, vol. 4, no. 9, p. 1799, Aug. 2008.

[23] W. Barthlott and C. Neinhuis, "Purity of the sacred lotus, or escape from contamination in biological surfaces," *Planta*, vol. 202, no. 1, pp. 1–8, Apr. 1997.

[24] R. Fürstner, W. Barthlott, C. Neinhuis, and P. Walzel, "Wetting and self-cleaning properties of artificial superhydrophobic surfaces.," *Langmuir ACS J. Surf. Colloids*, vol. 21, no. 3, pp. 956–61, Feb. 2005.

[25] A. Nakajima, K. Hashimoto, T. Watanabe, K. Takai, G. Yamauchi, and A. Fujishima, "Transparent Superhydrophobic Thin Films with Self-Cleaning Properties," *Langmuir*, vol. 16, no. 17, pp. 7044–7047, Aug. 2000.

[26] Z. Guo, W. Liu, and B.-L. Su, "Superhydrophobic surfaces: from natural to biomimetic to functional.," *J. Colloid Interface Sci.*, vol. 353, no. 2, pp. 335–55, Jan. 2011.

[27] V. Zorba *et al.*, "Biomimetic Artificial Surfaces Quantitatively Reproduce the Water Repellency of a Lotus Leaf," *Adv. Mater.*, vol. 20, no. 21, pp. 4049–4054, Nov. 2008.

[28] L. Zhang, Z. Zhou, B. Cheng, J. M. Desimone, and E. T. Samulski, "Superhydrophobic behavior of a perfluoropolyether lotus-leaf-like topography.," *Langmuir ACS J. Surf. Colloids*, vol. 22, no. 20, pp. 8576–80, Sep. 2006.

[29] B. Bhushan, Y. C. Jung, and K. Koch, "Micro-, nano- and hierarchical structures for superhydrophobicity, self-cleaning and low adhesion.," *Philos. Transact. A Math. Phys. Eng. Sci.*, vol. 367, no. 1894, pp. 1631–72, May 2009.

[30] P. Martins, A. C. Lopes, and S. Lanceros-Mendez, "Electroactive phases of poly(vinylidene fluoride): Determination, processing and applications," *Prog. Polym. Sci.*, vol. 39, no. 4, pp. 683–706, Apr. 2014.

[31] S. Wu, "Calculation of interfacial tension in polymer systems," *J. Polym. Sci. Part C Polym. Symp.*, vol. 34, no. 1, pp. 19–30, Mar. 2007.

[32] E. I. Vargha-Butler, T. K. Zubovits, H. A. Hamza, and A. W. Neumann, "Surface Tension Effects in the Sedimentation of Polymer Particles in Various Liquid Mixtures," *J. Dispers. Sci. Technol.*, vol. 6, no. 3, pp. 357–379, Jan. 1985.

[33] A. B. D. Cassie and S. Baxter, "Wettability of porous surfaces," *Trans. Faraday Soc.*, vol. 40, no. 0, pp. 546–551, Jan. 1944.

[34] Z. R. Zheng, Z. Y. Gu, R. T. Huo, and Y. H. Ye, "Superhydrophobicity of polyvinylidene fluoride membrane fabricated by chemical vapor deposition from solution," *Appl. Surf. Sci.*, vol. 255, pp. 7263–7267, 2009.

[35] F. J. Wang, S. Lei, J. F. Ou, M. S. Xue, and W. Li, "Superhydrophobic surfaces with excellent mechanical durability and easy repairability," *Appl. Surf. Sci.*, vol. 276, pp. 397–400, 2013.

[36] Z. R. Zheng, Z. Y. Gu, R. T. Huo, and Z. S. Luo, "Superhydrophobic poly(vinylidene fluoride) film fabricated by alkali treatment enhancing chemical bath deposition," *Appl. Surf. Sci.*, vol. 256, pp. 2061–2065, 2010.

[37] H. Wang *et al.*, "A robust superhydrophobic PVDF composite coating with wear/corrosion-resistance properties," *Appl. Surf. Sci.*, vol. 332, no. 0, pp. 518–524, 2015.

[38] Z. Zheng, Z. Gu, R. Huo, and Z. Luo, "Fabrication of self-cleaning poly(vinylidene fluoride) membrane with micro/nanoscaled two-tier roughness," *J. Appl. Polym. Sci.*, vol. 122, no. 2, pp. 1268–1274, Oct. 2011.

[39] D. A. Zha, S. L. Mei, Z. Y. Wang, H. J. Li, Z. J. Shi, and Z. X. Jin, "Superhydrophobic polyvinylidene fluoride/graphene porous materials," *Carbon*, vol. 49, pp. 5166–5172, 2011.

[40] T. F. Wu, Y. Z. Pan, and L. Li, "Fabrication of superhydrophobic hybrids from multiwalled carbon nanotubes and poly(vinylidene fluoride)," *Colloids Surf. -Physicochem. Eng. Asp.*, vol. 384, pp. 47–52, 2011.

[41] R. Li, C. B. Chen, J. Li, L. M. Xu, G. Y. Xiao, and D. Y. Yan, "A facile approach to superhydrophobic and superoleophilic graphene/polymer aerogels," *J. Mater. Chem. A*, vol. 2, pp. 3057–3064, 2014.

[42] Y. L. Peng, H. W. Fan, J. Ge, S. B. Wang, P. Chen, and Q. Jiang, "The effects of processing conditions on the surface morphology and hydrophobicity of polyvinylidene fluoride membranes prepared via vapor-induced phase separation," *Appl. Surf. Sci.*, vol. 263, pp. 737–744, 2012.

[43] L. Yan, K. Wang, and L. Ye, "Super hydrophobic property of PVDF/CaCO 3 nanocomposite coatings," *J. Mater. Sci. Lett.*, vol. 22, no. 23, pp. 1713–1717, Dec. 2003.

[44] M. Li *et al.*, "Controlling the microstructure of poly(vinylidene-fluoride) (PVDF) thin films for microelectronics," *J. Mater. Chem. C*, vol. 1, no. 46, p. 7695, Nov. 2013.

[45] C. Boo, J. Lee, and M. Elimelech, "Omniphobic Polyvinylidene Fluoride (PVDF) Membrane for Desalination of Shale Gas Produced Water by Membrane Distillation," *Environ. Sci. Technol.*, vol. 50, no. 22, pp. 12275–12282, Nov. 2016.

[46] L. Brockway and H. Taylor, "A statistical model for the wettability of surfaces with heterogeneous pore geometries," *Mater. Res. Express*, vol. 3, no. 10, p. 105039, 2016.

[47] A. F. Stalder, T. Melchior, M. Müller, D. Sage, T. Blu, and M. Unser, "Low-bond axisymmetric drop shape analysis for surface tension and contact angle measurements of sessile drops," *Colloids Surf. Physicochem. Eng. Asp.*, vol. 364, no. 1–3, pp. 72–81, Jul. 2010.

[48] A. F. Stalder, G. Kulik, D. Sage, L. Barbieri, and P. Hoffmann, "A snake-based approach to accurate determination of both contact points and contact angles," *Colloids Surf. Physicochem. Eng. Asp.*, vol. 286, no. 1–3, pp. 92–103, Sep. 2006.

[49] "ImageJ." [Online]. Available: https://imagej.nih.gov/ij/. [Accessed: 11-Jul-2016].

[50] K. S. Birdi, *Surface Chemistry Essentials*. CRC Press, 2013.

[51] G. Korosi and E. S. Kovats, "Density and surface tension of 83 organic liquids," *J. Chem. Eng. Data*, vol. 26, no. 3, pp. 323–332, Jul. 1981.

[52] H. Matsuyama, M. Teramoto, R. Nakatani, and T. Maki, "Membrane formation via phase separation induced by penetration of nonsolvent from vapor phase. I. Phase diagram and mass transfer process," *J. Appl. Polym. Sci.*, vol. 74, no. 1, pp. 159–170, Oct. 1999.

[53] H. Matsuyama, M. Teramoto, R. Nakatani, and T. Maki, "Membrane formation via phase separation induced by penetration of nonsolvent from vapor phase. II. Membrane morphology," *J. Appl. Polym. Sci.*, vol. 74, no. 1, pp. 171–178, Oct. 1999.

[54] G. R. Guillen, Y. Pan, M. Li, and E. M. V. Hoek, "Preparation and Characterization of Membranes Formed by Nonsolvent Induced Phase Separation: A Review," *Ind. Eng. Chem. Res.*, vol. 50, no. 7, pp. 3798–3817, Apr. 2011.

[55] A. Chapiro, Z. Mankowski, and N. Schmitt, "Unusual swelling behavior of films of polyvinyl- and polyvinylidene/fluorides in various solvents," *J. Polym. Sci. Polym. Chem. Ed.*, vol. 20, no. 7, pp. 1791–1796, Jul. 1982.

[56] R. N. Wenzel, "Resistance of Solid Surfaces to Wetting by Water," *Ind. Eng. Chem.*, vol. 28, no. 8, pp. 988–994, Aug. 1936.

[57] L. Brockway and H. Taylor, "A nanoporous, ultrahydrophobic aluminum-coating process with exceptional dropwise condensation and shedding properties," *Mater. Res. Express*, vol. 4, no. 4, p. 45003, 2017.

[58] A. Tuteja *et al.*, "Designing Superoleophobic Surfaces," *Science*, vol. 318, no. 5856, pp. 1618–1622, Dec. 2007.

[59] E. Bormashenko *et al.*, "Contact Angle Hysteresis on Polymer Substrates Established with Various Experimental Techniques, Its Interpretation, and Quantitative Characterization," *Langmuir*, vol. 24, no. 8, pp. 4020–4025, Apr. 2008.

[60] G. McHale, N. J. Shirtcliffe, and M. I. Newton, "Contact-Angle Hysteresis on Super-Hydrophobic Surfaces," *Langmuir*, vol. 20, no. 23, pp. 10146–10149, Nov. 2004.